AFRL-RQ-WP-TP-2016-0079

FLOW PATTERN IDENTIFICATION OF HORIZONTAL TWO-PHASE REFRIGERANT FLOW USING NEURAL NETWORKS (POSTPRINT)

Abdeel J. Roman and Larry W. Byrd

Mechanical and Thermal Systems Branch
Power and Control Division

Jamie S. Ervin and Michael S. Hanchak

University of Dayton Research Institute

Paul J. Kreitzer

UES, Inc.

DECEMBER 2015

AIR FORCE RESEARCH LABORATORY
AEROSPACE SYSTEMS DIRECTORATE
WRIGHT-PATTERSON AIR FORCE BASE, OH 45433-7541
AIR FORCE MATERIEL COMMAND
UNITED STATES AIR FORCE

NOTICE AND SIGNATURE PAGE

*//Signature//   //Signature//

TRAVIS E. MICHALAK   THOMAS L. REITZ, Chief
Program Manager   Mechanical and Thermal Systems Branch
Mechanical and Thermal Systems Branch   Power and Control Division
Power and Control Division   Aerospace Systems Directorate

REPORT DOCUMENTATION PAGE

1. REPORT DATE *(DD-MM-YY)*	2. REPORT TYPE	3. DATES COVERED *(From - To)*
December 2015	Journal Article Postprint	01 October 2013 – 22 June 2015

4. TITLE AND SUBTITLE

FLOW PATTERN IDENTIFICATION OF HORIZONTAL TWO-PHASE REFRIGERANT FLOW USING NEURAL NETWORKS (POSTPRINT)

5a. CONTRACT NUMBER
In-house

5b. GRANT NUMBER

5c. PROGRAM ELEMENT NUMBER
62203F

6. AUTHOR(S)

Abdeel J. Roman and Larry W. Byrd (AFRL/RQQM)
Jamie S. Ervin and Michael S. Hanchak (University of Dayton Research Institute)
Paul J. Kreitzer (UES, Inc.)

5d. PROJECT NUMBER
3145

5e. TASK NUMBER

5f. WORK UNIT NUMBER
Q0LA

7. PERFORMING ORGANIZATION NAME(S) AND ADDRESS(ES)

Mechanical and Thermal Systems Branch (AFRL/RQQM)
Power and Control Division
Air Force Research Laboratory, Aerospace Systems Directorate
Wright-Patterson Air Force Base, OH 45433-7541
Air Force Materiel Command, United States Air Force

University of Dayton Research Institute
300 College Park Avenue
Dayton, OH 45469

UES, Inc.
4401 Dayton-Xenia Road
Dayton, OH 45432

8. PERFORMING ORGANIZATION REPORT NUMBER
AFRL-RQ-WP-TP-2016-0079

9. SPONSORING/MONITORING AGENCY NAME(S) AND ADDRESS(ES)

Air Force Research Laboratory
Aerospace Systems Directorate
Wright-Patterson Air Force Base, OH 45433-7541
Air Force Materiel Command
United States Air Force

10. SPONSORING/MONITORING AGENCY ACRONYM(S)
AFRL/RQQM

11. SPONSORING/MONITORING AGENCY REPORT NUMBER(S)
AFRL-RQ-WP-TP-2016-0079

12. DISTRIBUTION/AVAILABILITY STATEMENT
Approved for public release; distribution unlimited.

13. SUPPLEMENTARY NOTES
PA Case Number: 88ABW-2015-3165; Clearance Date: 22 June 2015.
Paper published in *International Communications in Heat and Mass Transfer*, Vol. 71, Elsevier, 2016, pp. 254-264.
© 2015 Elsevier Ltd. The U.S. Government is joint author of the work and has the right to use, modify, reproduce, release, perform, display, or disclose the work.

14. ABSTRACT

In this work, electrical capacitance tomography (ECT) and neural networks were used to automatically identify two-phase flow patterns for refrigerant R-134a flowing in a horizontal tube. In laboratory experiments, high-speed images were recorded for human classification of liquid–vapor flow patterns. The corresponding permittivity data obtained from tomograms was then used to train feedforward neural networks to recognize flow patterns. An objective was to determine which subsets of data derived from tomograms could be used as input data by a neural network to classify nine liquid–vapor flow patterns. Another objective was to determine which subsets of input data provide high identification success when analyzed by a neural network. Transitional flow patterns associated with common horizontal flow patterns were considered. A unique feature of the current work was the use of the vertical center of mass coordinate in pattern classification. The highest classification success rates occurred using neural network input which included the probability density functions (in time) for both spatially averaged permittivity and center of mass location in addition to the four statistical moments (in time) for spatially averaged permittivity data. The combination of these input data resulted in an average success rate of 98.1% for nine flow patterns. In addition, 99% of the experimental runs were either correctly classified or misclassified by only one flow pattern.

15. SUBJECT TERMS electrical capacitance tomography, neural network, refrigerant, two-phase flow

16. SECURITY CLASSIFICATION OF:			17. LIMITATION OF ABSTRACT:	18. NUMBER OF PAGES	19a. NAME OF RESPONSIBLE PERSON (Monitor)
a. REPORT Unclassified	**b. ABSTRACT** Unclassified	**c. THIS PAGE** Unclassified	SAR	14	Travis A. Michalak
					19b. TELEPHONE NUMBER *(Include Area Code)* N/A

Flow pattern identification of horizontal two-phase refrigerant flow using neural networks ☆

Abdeel J. Roman [a], Paul J. Kreitzer [b], Jamie S. Ervin [c,*], Michael S. Hanchak [c], Larry W. Byrd [a]

[a] Air Force Research Laboratory, Wright-Patterson AFB, OH 45433, USA
[b] UES Inc., Dayton, OH 45432, USA
[c] University of Dayton Research Institute, Dayton, OH 45469-0044, USA

ARTICLE INFO

ABSTRACT

In this work, electrical capacitance tomography (ECT) and neural networks were used to automatically identify two-phase flow patterns for refrigerant R-134a flowing in a horizontal tube. In laboratory experiments, high-speed images were recorded for human classification of liquid–vapor flow patterns. The corresponding permittivity data obtained from tomograms was then used to train feedforward neural networks to recognize flow patterns. An objective was to determine which subsets of data derived from tomograms could be used as input data by a neural network to classify nine liquid–vapor flow patterns. Another objective was to determine which subsets of input data provide high identification success when analyzed by a neural network. Transitional flow patterns associated with common horizontal flow patterns were considered. A unique feature of the current work was the use of the vertical center of mass coordinate in pattern classification. The highest classification success rates occurred using neural network input which included the probability density functions (in time) for both spatially averaged permittivity and center of mass location in addition to the four statistical moments (in time) for spatially averaged permittivity data. The combination of these input data resulted in an average success rate of 98.1% for nine flow patterns. In addition, 99% of the experimental runs were either correctly classified or misclassified by only one flow pattern.

© 2015 Elsevier Ltd. All rights reserved.

1. Introduction

Understanding the two-phase flow behavior of refrigerants is important for the design of advanced aircraft cooling systems. Specifically, the classification of liquid–vapor structures into flow patterns is useful for predicting heat transfer rates and, ultimately, system performance. Most flow and heat transfer correlations require a priori knowledge of the two-phase flow pattern and are based on steady-state conditions [1,2]. Although flow pattern identification can be performed using high-speed imaging, this method generally relies on the visual interpretation of liquid–vapor patterns. Unfortunately, visual interpretation can be highly subjective [2]. As a consequence, numerous flow pattern classifications have been defined in the past [3–7]. In contrast to visual observation, which is often impractical, non-visual sensor signals can be analyzed to provide more objective classifications. Moreover, sensor signals are desired as inputs to real-time modeling and control.

Capacitance techniques are non-invasive and rely on differences in electrical permittivity to distinguish between liquid and vapor phases [2,8–9]. Capacitance measurements acquired simultaneously with high-speed videos of air-water flows have been used to identify two-phase flow patterns [2]. In addition, encouraging results involving the identification of two-phase flow patterns of refrigerants have been obtained using a capacitance probe that produced void fraction signals [10]. However, a single capacitance probe (as in [2,10]) may not fully characterize the liquid–vapor spatial distribution within a flow passage. This could lead to incorrect assumptions about the actual flow behavior. In contrast, electrical capacitance tomography (ECT) can provide a nearly instantaneous view of the liquid–vapor distribution within the system without optical access. Tomography may be used to derive the permittivity distribution from capacitance data [8,9]. The permittivity distribution, in turn, can provide the spatial distribution of the liquid and vapor phases. Many past research efforts involving ECT have focused on industrial applications where qualitative results were sufficient [8]. The use of ECT in detailed studies of liquid and vapor in horizontal flow has been limited, much less with the use of dielectric refrigerants which are of interest here [8,10,11].

Artificial neural networks are used for pattern recognition and trend prediction involving complex processes. In an artificial neural network, the neurons (often called nodes) receive input signals, and each node calculates an individual output using a weighted sum and nonlinear activation function. Learning is achieved by the adjustment of these weights [12]. Past studies suggest that there is potential for using a

---

Nomenclature

A_i	Individual pixel area [m^2]
A_T	Sum of all pixel areas [m^2]
D	Tube diameter [m]
D_b	Bubble diameter [m]
ECT	Electrical capacitance tomography
L	Length [m]
PDF	Probability density function
t	Time [s]
$y_c(t)$	Center of mass vertical coordinate normalized by the tube diameter
$y_c(t)_{PDF}$	Probability density function for center of mass (normalized) vertical coordinate
y_i	Vertical coordinate normalized by the tube diameter for the ith pixel
$\varepsilon(\tilde{x},t)$	Permittivity determined by tomography [F/m]
ε_f	Liquid permittivity [F/m]
ε_g	Vapor permittivity [F/m]
$\varepsilon^*(\tilde{x},t)$	Normalized permittivity
$\overline{\varepsilon^*}(t)$	Spatial average of normalized permittivity
$\overline{\varepsilon^*}(t)_{PDF}$	Probability density function of $\overline{\varepsilon^*}(t)$
$\varepsilon_i^*(\tilde{x},t)$	Normalized permittivity for an individual pixel
$\langle\overline{\varepsilon^*}(t)\rangle$	Time averaged $\overline{\varepsilon^*}(t)$
$\langle\overline{\varepsilon^*}(t)\rangle_{KURT}$	Kurtosis of time averaged $\overline{\varepsilon^*}(t)$
$\langle\overline{\varepsilon^*}(t)\rangle_{SKEW}$	Skewness of time averaged $\overline{\varepsilon^*}(t)$
$\overline{\varepsilon^*}(t)_{VAR}$	Variance of time averaged $\overline{\varepsilon^*}(t)$
$\tilde{x}$	Spatial locations, x and y [m]

neural network to objectively classify liquid–vapor distribution data [13–15]. These studies have used measured or simulated impedance (conductance) signals rather than input from ECT [13–16]. In addition, nearly all previous flow identification studies that have used neural networks were performed for vertical flows.

In this paper, the use of ECT together with neural networks to identify liquid–vapor flow patterns is explored. For this purpose, experiments involving the horizontal flow of refrigerant R-134a through a tube of small diameter (7 mm) were conducted. A horizontal-two phase flow can be categorized into one of several flow patterns which may include bubbly, plug, slug, stratified-wavy, and annular flows [17]. Here, previous work is extended by including additional transitional flow patterns corresponding to four of the above flow patterns

for horizontal flow. The names of the transitional flow patterns are derived from these four flow patterns and are given here as the bubbly-transitional, plug-transitional, slug-transitional, and stratified-wavy-transitional patterns. In the current work, high-speed images of the flow patterns were recorded for purposes of initial human classification and final training verification. Processed permittivity data obtained from two-dimensional tomograms was used to train neural networks. A goal was to classify nine horizontal two-phase flow patterns with reasonable speed using neural networks as a predictive tool. Input information for the neural networks included the spatially averaged permittivity, center of mass location, and their probability density functions (in time). It also included four statistical moments (in time) for spatially averaged permittivity data. Another objective was to determine which subsets of input data provide high identification success for the flow patterns when analyzed by a neural network.

2. Experimental setup

To explore the use of ECT in the identification of two-phase flow patterns, laboratory experiments were performed in which liquid–vapor flow patterns were generated for flow in a horizontal tube. Fig. 1 shows a schematic of the experimental arrangement in which liquid R-134a was pumped through a heater to produce two-phase flow. To obtain different liquid–vapor flow patterns, the volumetric flow rates were adjusted in the range 0.1 to 0.5 L/min, while varying the heater power between 0 and 500 W. Downstream from the heated section, the two-phase flow entered a fused quartz observation section (tube with 7 mm ID). The observation section permitted imaging using a high speed video camera (Phantom V4.2) and had thermocouples and pressure transducers located at 1.2 m increments along its length. The high speed camera was used to compare actual images of liquid–vapor flow with ECT characterization. R-134a passed through the cylindrical ECT sensor (ITS, 0690). Fig. 1 shows one flow path for R-134a and another for cooling water which was used to condense R-134a vapor in the condenser (Lytron, LL510G02). The water was cooled by a chiller (PolyScience, 4260 T).

Table 1 lists the measurement uncertainties associated with the thermocouples, pressure transducers (Omega PX-409), and flow meter (McMillan) shown in Fig. 1. Experiments were performed with the refrigerant saturation conditions at the ambient temperature of 20 °C. Relatively small temperature differences (~1 °C) between the ambient and refrigerant in the observation section of tubing provided reasonable grounds to neglect the heat transfer between them.

The ECT system consists of a multi-electrode sensor, electronics for capacitance determination, and data acquisition components [18]. The
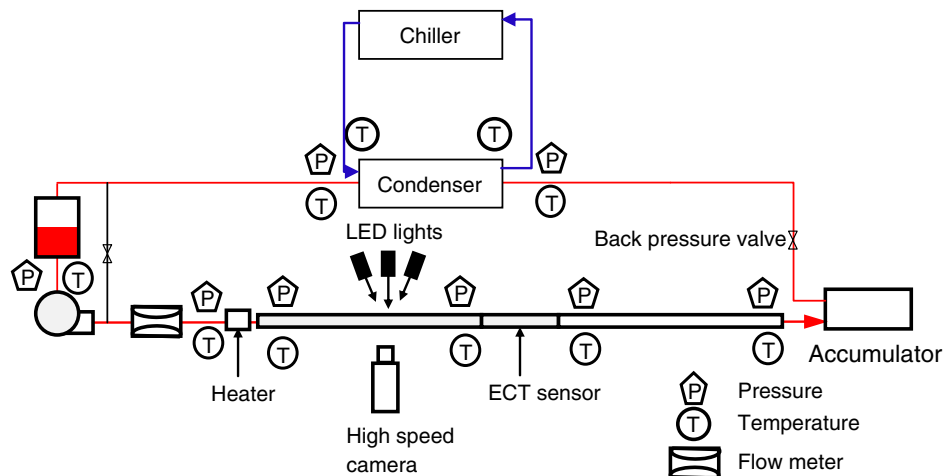

Fig. 1. Schematic of two phase flow system. Red represents the refrigerant, and blue represents chilled water.

Table 1
Measurement uncertainties.

Instrument	Type	Calibration range	Uncertainty
Thermocouple	Type T	5–100 °C	± 0.1 °C
Pressure transducer	Gauge	0–1034 kPa	± 0.3 kPa
Flow meter	Turbine	0.10–1.00 L/min	± 0.005 L/min

sensor fits around a section of the flow passage and measures changes in capacitance values between electrode pairs. Fig. 2a shows the configuration for eight electrodes (51 mm length), insulation, grounded screen, and measurement volume. Starting with electrode one, a voltage signal was applied to it. The capacitance was then measured from the remaining electrodes, two through eight. Next, electrode two became electrified, and electrodes three through eight were used to measure the capacitance. This process was repeated around the sensor until all (28) pairs of measurements were completed. A single tomogram was generated from these 28 capacitance measurements. In addition, a sensing unit conditioned the sensor signals and transmitted them to a data acquisition system. Details of the hardware and experimental procedures are available elsewhere [19].

Each tomogram provided a two-dimensional representation of the permittivity obtained from capacitance values at each sample time. Since the internal sensor volume encompassed a portion (51 mm) of the flow path, the two-dimensional permittivity values were calculated from a three-dimensional measurement volume and averaged in time. Thus, the sensor length along the flow path as well as the sampling rate were practical limits for the sensor resolution. At the sampling rate of ~48 Hz, 20 ms was necessary to acquire the data necessary for one two-dimensional tomogram with a delay of 1 ms between data sets. In this period, a two-phase feature with a speed of ~1 m/s would be detected by the sensor two times before leaving the sensing area. In the present experiments, the greatest velocity of a vapor feature was ~0.85 m/s. Thus, the sampling rate was reasonable.

Eq. (1) below was used to normalize the permittivity, $\varepsilon(\tilde{x}, t)$, that was determined by tomographic reconstruction. Here, $\tilde{x}$ represents the spatial variables, x and y, and t is time. This normalization assigns $\varepsilon^*(\tilde{x}, t)$ to be zero for only vapor (ε_g) and one for liquid (ε_f) alone. Since non-linear electric field responses may generate values outside the normalized

range, a baseline reference value (ε_f or ε_g) was recorded while the sensor contained only liquid (ε_f) or only vapor (ε_g). A tomogram may have regions that are assigned values of $\varepsilon^*(\tilde{x}, t)$ between zero and one since a given pixel may represent a liquid–vapor mixture.

$$\varepsilon^*(\tilde{x}, t) = (\varepsilon(\tilde{x}, t) - \varepsilon_g)/(\varepsilon_f - \varepsilon_g) \tag{1}$$

In this work, the linear back projection algorithm was used in the software provided by the instrument manufacturer for the tomographic reconstruction. This two-dimensional (cross-sectional) representation is proportional to $\varepsilon^*(\tilde{x}, t)$ within the sensor volume [18]. There are 812 pixels which comprise the computational domain for the reconstruction process (Fig. 2b). Since the cross-sectional area is circular, some elements were outside the circular boundary and not used. In addition, sensitivity maps generated by the manufacturer were used to linearize the measured capacitance values which were ultimately used in the reconstruction algorithm [18]. Subsequent processing of the tomograms was performed and is described in the next section of this paper.

Table 2 lists the flow patterns, heating rates, volumetric flow rates (at the pump outlet), pressure range, tube diameter, and time duration for each recorded flow pattern case. The experiments were conducted by holding the volumetric flow rate constant and incrementally increasing the heater power (Fig. 3). The heater power was held at a given value until the liquid–vapor behavior was steady or steady-periodic. Visual observations of the liquid–vapor behavior were made while recording ECT data. A total of 546 heater power and volumetric flow rate combinations were examined.

3. Data processing and analysis

Tomography was used to obtain $\varepsilon^*(\tilde{x}, t)$ from the capacitance measurements which, in turn, provided the two-dimensional distribution of the liquid and vapor phases within the section of tubing encompassed by the sensor. One issue concerning the tomographic data was to determine an acceptable number of input data to train the neural network in a reasonable time period (less than 10 min on a Dell Precision T7500 workstation, 64 bit dual processor). The required computational time was prohibitively large for directly using all 812 pixel values from each tomogram (500 tomograms were recorded for each run) for each
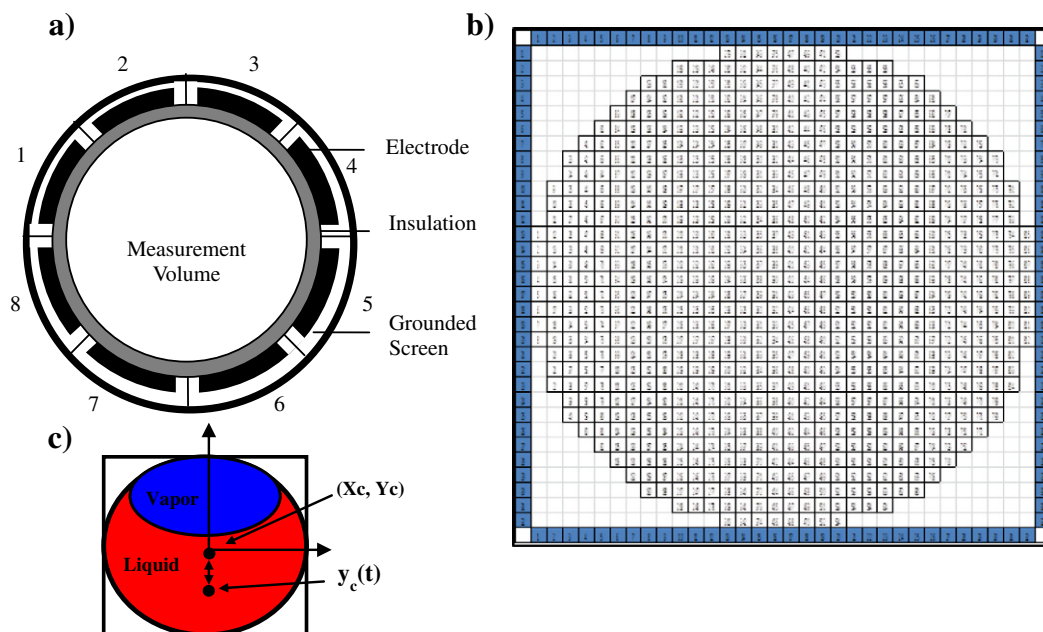
Fig. 2. Drawings of the a) cross-sectional view of the sensor with eight electrodes, b) tomography computational domain consisting of 812 pixels, and c) instantaneous normalized vertical coordinate ($y_c(t)$) corresponding to the refrigerant center of mass. The normalized coordinates (X_c, Y_c) designate the origin.

3

Table 2
Summary of two-phase flow experiments.

Common flow patterns	Bubble, plug, slug, strategy wavy, annular
Transitional flow patterns	Bubbly transitional, plug transitional, slug transitional, stratified wavy transitional
Heater power (W)	10–300
Heat flux, q'' (W/cm^2)	0.40–12
Volumetric flow rate (L/min)	0.10–0.50
Pressure (kPa)	500–800
Tube diameter (mm)	7
Duration of each observed flow pattern case (s)	30

of the 546 experimental runs as input data ($812 \times 500 \times 546 \sim 2.2 \times 10^8$ data points) to train a neural network. It was proposed that a combination of spatial- and time- averaging together with other quantities might allow for rapid training of accurate neural networks. Here, we explore the use of the following as input data for neural network flow pattern identification: the spatial average of $\varepsilon^*(\tilde{x}, t)$ (represented by $\overline{\varepsilon^*}(t)$), the probability density function of $\overline{\varepsilon^*}(t)$, the refrigerant local center of mass (i.e., the vertical coordinate normalized by the tube diameter and denoted by $y_c(t)$), and the probability density function of $y_c(t)$. In addition, the time average of $\overline{\varepsilon^*}(t)$ and the associated variance, kurtosis, and skewness values are considered.

$\overline{\varepsilon^*}(t)$ is given by Eq. (2), where A_i is the individual pixel area (Fig. 2b), $\varepsilon_i^*(\tilde{x}, t)$ is the normalized permittivity for an individual pixel, A_T is the sum of all (812) pixel areas, and t is time.

$$\overline{\varepsilon^*}(t) = \frac{1}{A_T} \sum_{i=1}^{812} \varepsilon_i^*(\tilde{x}, t) A_i \qquad (2)$$

A_i in Eq. (2) is identical for all pixels and, thus, $\overline{\varepsilon^*}(t)$ was obtained by taking the arithmetic mean of the $\varepsilon_i^*(\tilde{x}, t)$ values for each tomogram at a particular time, t. Since $\varepsilon^*(\tilde{x}, t)$ is unity for the presence of liquid alone and zero for vapor alone, $\overline{\varepsilon^*}(t)$ represents the time-varying liquid fraction in the sensor volume. Consequently, $1 - \overline{\varepsilon^*}(t)$ represents the time-varying void fraction.
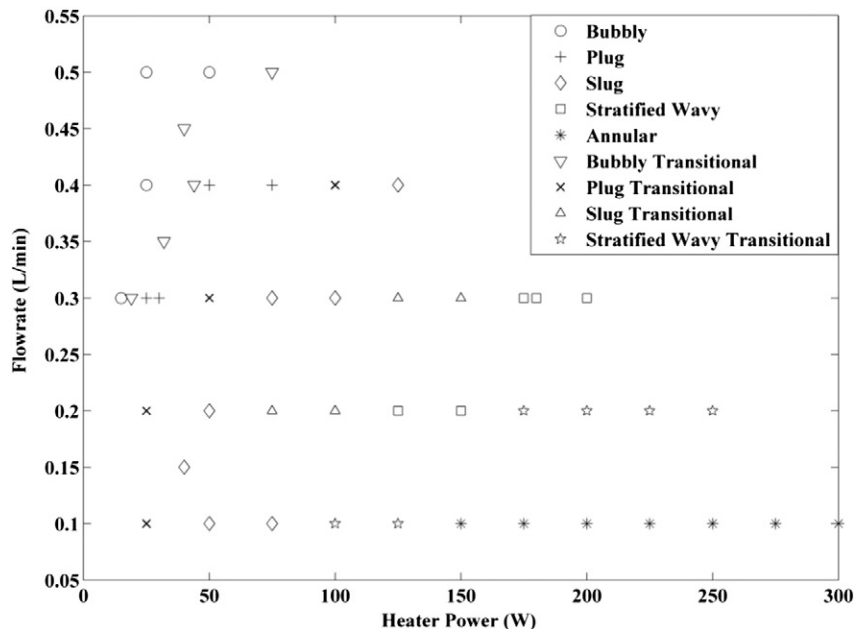
For each flow pattern test point (i.e., each heater power and volumetric flow rate combination), 500 tomograms were generated over a sampling period of 30 s. The probability density function (PDF) provided a way to observe the range of $\overline{\varepsilon^*}(t)$ occurring with time for a given case. Here, the PDF of $\overline{\varepsilon^*}(t)$ is denoted by $\overline{\varepsilon^*}(t)_{PDF}$. To estimate $\overline{\varepsilon^*}(t)_{PDF}$, MATLAB was used to first produce a histogram by separating the 500 values of $\overline{\varepsilon^*}(t)$ (obtained from the 500 tomograms) into bins [20]. Preliminary work showed that calculated histograms were sensitive to bin sizes below 25 but were insensitive to those in the range 25–100. Thus, 50 bins were used for determining all histograms. The estimate of $\overline{\varepsilon^*}(t)_{PDF}$ was then generated by a smooth fit to the histogram. In addition, MATLAB was used to estimate the time average, $\langle \overline{\varepsilon^*}(t) \rangle$, variance, $\langle \overline{\varepsilon^*}(t) \rangle_{VAR}$, skewness, $\langle \overline{\varepsilon^*}(t) \rangle_{SKEW}$, and kurtosis, $\langle \overline{\varepsilon^*}(t) \rangle_{KURT}$ of $\overline{\varepsilon^*}(t)$ using values from the 500 tomograms. $\langle \overline{\varepsilon^*}(t) \rangle$ provides a representative value for the time-varying void fraction, $\langle \overline{\varepsilon^*}(t) \rangle_{VAR}$ provides an indication of the fluctuation amplitude of $\langle \overline{\varepsilon^*}(t) \rangle$, and $\langle \overline{\varepsilon^*}(t) \rangle_{SKEW}$ provides a measure of the asymmetry of the probability density function. In terms of a physical interpretation, a time series that has numerous intermittent extreme events would have a relatively high $\langle \overline{\varepsilon^*}(t) \rangle_{KURT}$. Thus, a high kurtosis would, for example, be associated with the rapidly alternating occurrence of large vapor bubbles and liquid.

A running average was used to estimate the number of data samples required to obtain a stable time average [21]. The running average of $\overline{\varepsilon^*}(t)$ was used to determine an acceptable number of data points to estimate $\langle \overline{\varepsilon^*}(t) \rangle$. When the fluctuations in the running average were within a $\pm 5\%$ band of the stable average, the time average was assumed to be stable and the number of data points sufficient.

Since the vertical distribution of the liquid and vapor phases in a horizontal flow can be influenced by gravity, it may be advantageous to use the vertical coordinate of the center of mass, $y_c(t)$, of the tomogram (Fig. 2b) as a neural network input. Since the origin of the coordinate system is at the center of the tube, $y_c(t)$ is zero for a single phase flow within the tube. Because the positive direction for the y axis is up with respect to the gravity vector, a two-phase flow pattern will result in negative $y_c(t)$ values due to gravity drawing liquid to the bottom of the tube. $\varepsilon_i^*(\tilde{x}, t)$ and the densities of the saturated vapor (ρ_g) and liquid (ρ_f) were used to estimate the fluid mass associated with a given pixel for the center of mass calculation as given by Eq. (3). In Eq. (3), y_i represents a vertical pixel coordinate that is normalized by the tube diameter.

$$y_c(t) = \sum_{i=1}^{812} \left[\left(\rho_g + \varepsilon_i^*(\tilde{x}, t)\left(\rho_f - \rho_g\right)\right) y_i \right] \Big/ \sum_{i=1}^{812} \left[\rho_g + \varepsilon_i^*(\tilde{x}, t)\left(\rho_f - \rho_g\right)\right] \qquad (3)$$

Fig. 3. Visually observed flow patterns as a function of flow rate and heater power.

4

Following the calculation procedure with $\overline{\varepsilon^*}(t)$, PDFs for $y_c(t)$ were generated and are referred to as $y_c(t)_{PDF}$.

In this work, the MATLAB Neural Network package was used as the computational tool for identifying flow patterns. A feedforward neural network was selected for use due to its simplicity and ability to generalize to new situations [20]. This particular feedforward neural network had a hidden layer with nodes that used a sigmoid transfer function [20]. Training of a neural network was performed to identify the constants that comprise the weights and biases of each neuron. The number of hidden nodes was varied with different training sessions to determine an optimum number which would permit rapid calculations while avoiding overfitting. In this work, 50 was the maximum number of hidden nodes used. A single output layer was generated as a floating point number and rounded to the nearest integer value, corresponding to a flow pattern prediction.

The feedforward network together with the Levenberg-Marquardt training algorithm provide rapid calculation speed and are known for successful pattern identification [20]. Training was terminated when the generalization no longer improved which was indicated by an increase in the mean square error. The neural network was retrained by supplying it with additional randomized subsets of the original input and target data. This was repeated until the neural network predicted the observed flow patterns with an acceptable level of success, defined here to be the correct identification of flow patterns in at least 90% of the testing data. In the present work, the neural network was retrained up to twenty-five times to reach an acceptable level of success. The data used for testing were not part of the network training and, thus, provided an independent indication of neural network performance. That is, how well the network generalized beyond the supplied data [20]. Data from 546 experiments was randomly selected such that 30% were used for the validation and testing of a neural network, and 70% were used for training.

The neural network input included combinations of $\overline{\varepsilon^*}(t)$, $\overline{\varepsilon^*}(t)_{PDF}$, $\langle \overline{\varepsilon^*}(t) \rangle$, $\langle \overline{\varepsilon^*}(t) \rangle_{VAR}$, $\langle \overline{\varepsilon^*}(t) \rangle_{SKEW}$, $\langle \varepsilon^*(t) \rangle_{KURT}$, $y_c(t)$, and $y_c(t)_{PDF}$ derived from the tomograms. The number of values used for each neural network input depended on the type of data itself. The number of values used for $\overline{\varepsilon^*}(t)$, $\overline{\varepsilon^*}(t)_{PDF}$, $y_c(t)$, and $y_c(t)_{PDF}$ are described in the next section. The quantities $\langle \overline{\varepsilon^*}(t) \rangle$, $\langle \overline{\varepsilon^*}(t) \rangle_{VAR}$, $\langle \overline{\varepsilon^*}(t) \rangle_{SKEW}$, and $\langle \overline{\varepsilon^*}(t) \rangle_{KURT}$ were each a single value; they introduced four values for network training for each data set.

4. Results and discussion

In this section, the flow patterns are first characterized by high speed imaging. This is followed by a characterization of flow patterns by $\overline{\varepsilon^*}(t)$, $\overline{\varepsilon^*}(t)_{PDF}$, $y_c(t)$, and $y_c(t)_{PDF}$. The performance of the neural network inputs in classifying two-phase flow patterns is then described.

4.1. High speed imaging

High speed imaging was used for the initial human classification of the flow patterns. Table 3 shows representative images (view perpendicular to the tube axis) and cross-sectional drawings (view along the tube axis) for each flow pattern. It is useful to examine the images of Table 3 together with the plot in Fig. 3, which shows the dependence of the flow pattern on both the input heater power and volumetric flow rate. Generally, there were clear visual demarcations among the flow patterns. However, overlapping liquid–vapor behavior existed due to the stochastic nature of the transition patterns. Care was taken to label the transitions correctly, or, in the case of great uncertainty, eliminate them altogether. Lastly, Table 3 lists the time-averaged void fraction range for each flow pattern. As described earlier, the void fraction estimate is given by $1 - \langle \overline{\varepsilon^*}(t) \rangle$.

Table 3 shows a representative image of bubbly flow. Bubbly flow was the first flow pattern encountered after single-phase liquid flow as the heater power was increased from zero with the volumetric flow rate at the highest setting (Table 2, 0.5 L/min). As illustrated in Table 3 (drawing of view along tube axis), discrete bubbles with diameters (D_b) smaller than the tube radius ($D/2$) moved along the upper tube surface [17]. As the heater power was further increased at a constant flow rate (Fig. 3), bubbly flow evolved into what is termed bubbly transitional flow. The image of bubbly transitional flow in Table 3 is similar to that of bubbly flow but elongated bubbles move along the upper tube surface. The drawing along the tube axis indicates that D_b in the bubbly-transitional pattern were smaller than $D/2$, but the bubble length (L) could approach 2D.

Plug flow occurred when small adjacent bubbles coalesced into larger bubbles separated by liquid regions [17]. In addition, D_b continued to be smaller than D, but L was several D, and the bubble frequency increased significantly. Bubbles in plug-transitional flow (Table 3) have L and D_b similar to those in plug flow. However, plug-transitional bubbles have an elongated front section followed by a tail of smaller diameter. Slug flow evolved from plug transitional flow where L approached 80D. The bubbles had a consistent bullet shape with a rounded nose and tail. Also, D_b began to approach D. Liquid regions separated the vapor bubbles and often entrained small dispersed bubbles [17]. Slug-transitional flow is similar to slug flow in that the bubbles have a bullet shape with a short tail (not in image). However, L was greater than that for slug flow with smaller liquid regions.
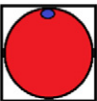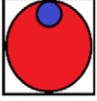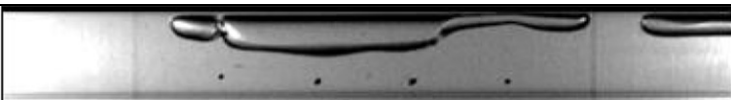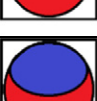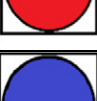
Stratified wavy flow occurred at high heater powers (Fig. 3). The image of stratified wavy flow shows that liquid slugs no longer occurred, and a vapor layer existed along the upper portion of the tube. Kelvin–Helmholtz instabilities are responsible for waves which propagated along the tube length, often contacting the upper tube surface [17,22]. As in stratified wavy flow, interfacial waves were also present in stratified wavy transitional flow. The waves were more frequent but their crests did not contact the upper tube surface. However, they rose up on the tube wall wetting the lateral surface [17,22]. Table 3 shows an example of annular flow consisting of liquid flow enveloping a flowing vapor core with small waves along the liquid–vapor interface. Annular flow is believed to occur when the vapor velocity increases beyond that in stratified wavy transitional flow [17,22]. The liquid layer is thicker at the bottom due to gravity and did not always extend all the way to the top.

4.2. $\overline{\varepsilon^*}$(t) and $\overline{\varepsilon^*}$(t)$_{PDF}$ characteristics for different flow patterns

The flow patterns are now described in terms of $\overline{\varepsilon^*}(t)$ and $\overline{\varepsilon^*}(t)_{PDF}$. Fig. 4 shows representative plots of $\overline{\varepsilon^*}(t)$ with time together with $\varep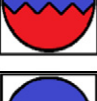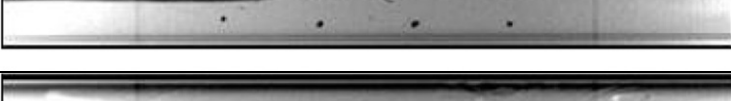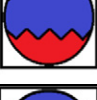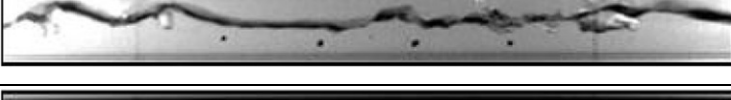silon^*(t)_{PDF}$ for nine flow patterns in the order of increasing void fraction. The plots correspond to the images, flow rates and heater powers of Table 3. Bubbly flow (Fig. 4a, flow rate of 0.5 L/min) has values of $\overline{\varepsilon^*}(t)$ in the range 0.95–1. $\overline{\varepsilon^*}(t)_{PDF}$ for bubbly flow (Fig. 4b) has a single peak near the upper end of the permittivity range, indicating that most of the flow is liquid. As the heater power increased at the flow rate of 0.5 L/min, bubbly transitional flow (Fig. 4c and d) resulted which had a broader $\overline{\varepsilon^*}(t)_{PDF}$ with lower values of $\overline{\varepsilon^*}(t)$. At a flow rate of 0.3 L/min and heater power near 30 W (Table 3), the $\overline{\varepsilon^*}(t)$ associated with plug flow (Fig. 4e) have a nearly periodic behavior with values ranging from 0.56 to 0.98. This nearly periodic behavior is confirmed by the image in Table 3 of flowing liquid plugs that are regularly separated by vapor. $\overline{\varepsilon^*}(t)_{PDF}$ for plug flow (Fig. 4f) has two distinguishable peaks for $\overline{\varepsilon^*}(t)$ of 0.78 and 0.93 due to the presence of large volumes of alternating liquid and vapor phases. The liquid plugs appear less periodic in the plug transitional flow pattern (Fig. 4g), and the corresponding $\overline{\varepsilon^*}(t)_{PDF}$ (Fig. 4h) is similar although broader than $\overline{\varepsilon^*}(t)_{PDF}$ for plug flow. Fig. 4i shows that $\overline{\varepsilon^*}(t)$ of the slug flow pattern has large, relatively rapid fluctuations that are associated with the passage of long vapor bubbles and short liquid slugs (Table 3). Fig. 4j shows that the $\overline{\varepsilon^*}(t)_{PDF}$ for slug flow, has a broad range. For slug transitional flow (Fig. 4k), the heights

5

Table 3
Representative flow pattern images and characteristics.

Flow pattern	Drawing of cross section viewed along tube axis	Representative image-viewed perpendicular to tube axis	Time averaged void fraction for flow pattern	Flow rate (L/min) for image	Heater power (W) for image
Bubbly			0.01–0.1	0.5	25
Bubbly - transitional			0.1–0.15	0.5	75
Plug			0.15–0.25	0.3	30
Plug - transitional			0.25–0.40	0.3	50
Slug			0.40–0.55	0.3	75
Slug - transitinal			0.55–0.60	0.3	125
Stratified wavy			0.60–0.65	0.3	180
Stratified wavy - transitional			0.65–0.75	0.2	250
Annular			0.75–0.95	0.1	300

of the peaks in $\overline{\varepsilon^*}(t)$ have generally increased and the $\overline{\varepsilon^*}(t)$ values in the $\overline{\varepsilon^*}(t)_{PDF}$ plot range from 0.21 to 0.98 (Fig. 4l). Relative to slug flow, this indicates sequential vapor bubbles with larger volumes that are separated by a greater distances. The $\overline{\varepsilon^*}(t)$ associated with stratified wavy flow (Fig. 4m) has large and small intermittent peaks relative to $\overline{\varepsilon^*}(t)$ of the slug and slug transitional patterns. The intermittent peaks are due to interfacial waves which propagated along the tube length (Table 3). Relative to stratified wavy flow, Fig. 4o shows that $\overline{\varepsilon^*}(t)$ for stratified wavy transitional flow has significantly smaller peaks. In addition, Fig. 4p shows that $\overline{\varepsilon^*}(t)_{PDF}$ is entirely below 0.5 which also means that the void fraction was always greater than 0.5. The amplitude of the fluctuations in $\overline{\varepsilon^*}(t)$ for annular flow is small (Fig. 4q) relative to those of stratified wavy or stratified wavy transitional flows. This is confirmed by the observation that interfacial waves were no longer visible

(Table 3). In addition, the plot of $\overline{\varepsilon^*}(t)_{PDF}$ for annular flow has a peak with no tail which accompanies a large void fraction (Table 3). This might be anticipated from the images of a flowing vapor core and liquid annulus within the tube (Table 3) for these flow patterns.

4.3. $y_c(t)$, and $y_c(t)_{PDF}$ Characteristics for different flow patterns

For a liquid–vapor flow that is horizontal with respect to gravity, the gas phase is near the upper surface of the flow passage with the liquid phase below if the tube is long enough for the vapor to stratify. Consequently, it is helpful to use the vertical coordinate of the tomogram centroid location as a neural network input. Fig. 5 shows $y_c(t)$, and $y_c(t)_{PDF}$ for each flow pattern. For reference, a y-coordinate value of 0 corresponds to the center of the tube. The peaks and troughs

6

of $y_c(t)$ in Fig. 5 generally track with those of $\overline{\varepsilon^*}(t)$ in Fig. 4 for the corresponding patterns. This occurs for two reasons. The first is that the center of mass shifts downward (upward) as the vapor fraction increases (decreases) due to the difference in phase densities in a

gravity field. The second reason is that $\overline{\varepsilon^*}(t)$ decreases with increasing vapor volume. Figs. 4 and 5 show that $\overline{\varepsilon^*}(t)_{PDF}$ and $y_c(t)_{PDF}$ both broaden beyond a single peak and then ultimately return to a single peak from bubbly to annular flows.
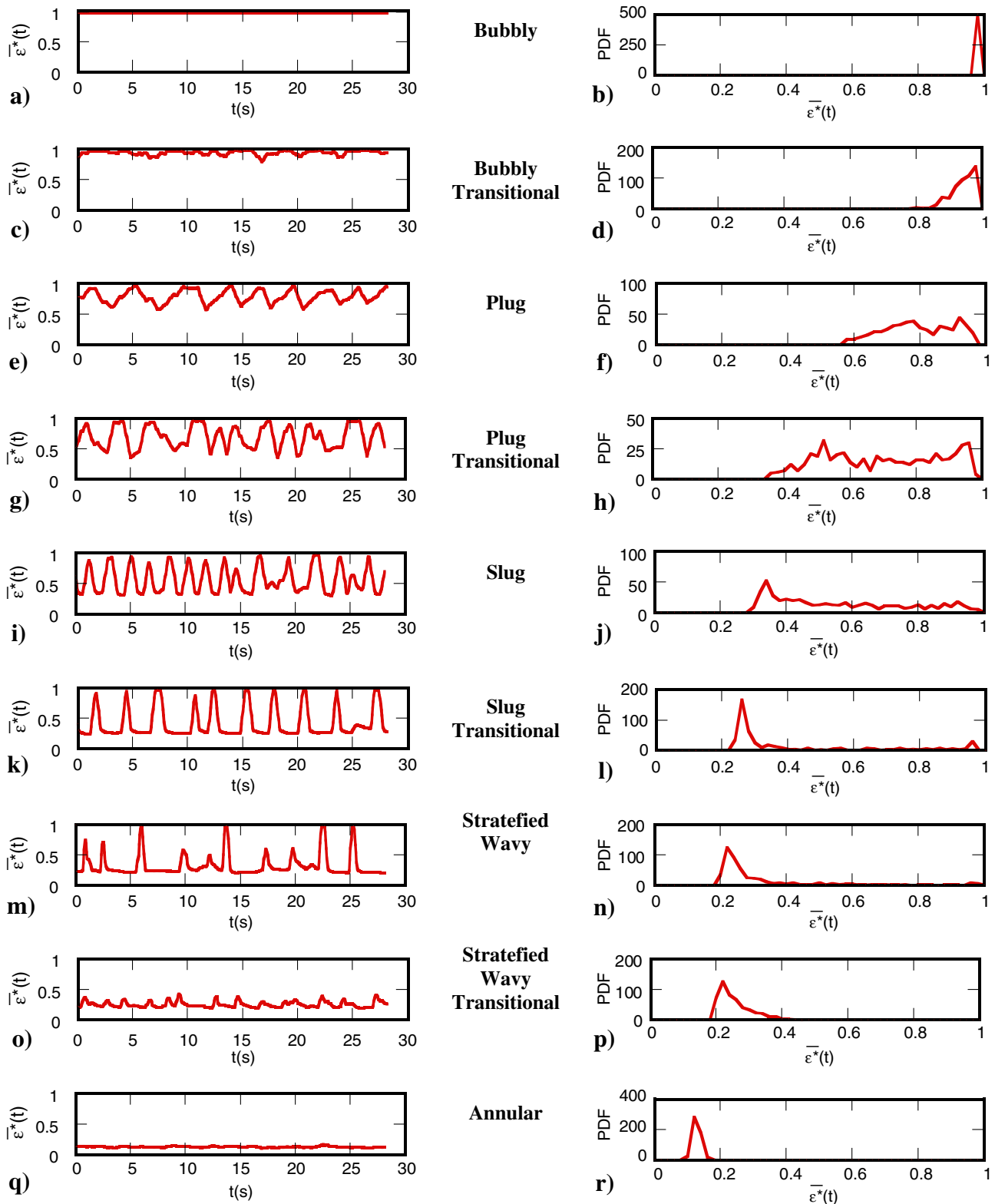
Fig. 4. Plots of $\overline{\varepsilon^*}(t)$ and $\overline{\varepsilon^*}(t)_{PDF}$ for bubbly (a and b), bubbly transitional (c and d), plug (e and f), plug transitional (g and h), slug (i and j), slug transitional (k and l), stratefied wavy (m and n), stratefied wavy transitional (o and p), and annular (q and r) flows.

Fig. 5. $y_c(t)$ and $y_c(t)_{PDF}$ behavior for bubbly (a and b), bubbly transitional (c and d), plug (e and f), plug transitional (g and h), slug (i and j), slug transitional (k and l), stratified wavy (m and n), stratified wavy transitional (o and p), and annular (q and r) flows.

4.4. Neural network studies

It is useful to determine which combinations of input data types derived from ECT tomograms allow rapid, classification of two-phase flow patterns by a feedforward neural network. The current study was carried out in two stages with increasing complexity. In the first, bubbly, plug, slug, stratified-wavy, and annular patterns were considered since they are relatively well defined and have been treated elsewhere [17, 22]. It was proposed that combinations of input data types that resulted in high success rates for classifying flow patterns in the first stage could

8

then be used in the second, more challenging stage to identify nine flow patterns.

Table 4 compares the classification success rates for eight neural network input vectors for the five basic flow patterns used in the first stage of this study. The first column provides the flow pattern category, and the second lists the number of experimental runs for each flow pattern. The third through the tenth columns provide the classification success rates for input that was comprised of individual and combined data types. Here, the success rate is defined as the percentage of flow patterns predicted correctly. Based on past work involving vertical flows and other instrumentation, there was reason to believe that the use of neural network input values derived from time averaging or probability density functions have potential for reasonable success rates [13,14]. Thus, the seventh column lists the success rates for flow pattern identification that used $\langle\overline{\varepsilon^*}(t)\rangle$, $\langle\overline{\varepsilon^*}(t)\rangle_{VAR}$, $\langle\overline{\varepsilon^*}(t)\rangle_{SKEW}$, and $\langle\overline{\varepsilon^*}(t)\rangle_{KURT}$, together as input for each experiment. Similarly, columns 8 through 10 list the success rates for input comprised of $\langle\overline{\varepsilon^*}(t)\rangle$, $\langle\overline{\varepsilon^*}(t)\rangle_{VAR}$, $\langle\overline{\varepsilon^*}(t)\rangle_{SKEW}$, and $\langle\overline{\varepsilon^*}(t)\rangle_{KURT}$ with $\overline{\varepsilon^*}(t)_{PDF}$ and/or $y_c(t)_{PDF}$ for each experimental run. The second row in Table 4 provides the number of input data points for each data type. The bottom row lists the average success rate of the neural network resulting from the use of different input data types.

Table 4 shows that using either $\overline{\varepsilon^*}(t)$ or $y_c(t)$ alone as an input resulted in the lowest overall success rates with the least success in defining slug flow. The use of other input types provided success rates greater than 90% for all flow patterns. Since a success rate of 90% or greater is a goal, Table 4 shows that it is acceptable to use any listed input other than $\overline{\varepsilon^*}(t)$ or $y_c(t)$ to identify the basic flow patterns. The average classification success rate over all patterns for columns 5 and 7 shows that the first four statistical (time) moments involving $\overline{\varepsilon^*}(t)$ provide information that is only slightly better than that of $\overline{\varepsilon^*}(t)_{PDF}$. This supports the conclusion of Rosa et al. [13] that the first four statistical (time) moments involving $\overline{\varepsilon^*}(t)$ provide information essentially equivalent to that of $\overline{\varepsilon^*}(t)_{PDF}$.

The bubbly, plug, slug, and stratified-wavy flow patterns were then subdivided into categories which included transition patterns. In these transition regions the flow may oscillate between the adjacent patterns making classification difficult. Consequently, Table 5 shows neural network classification results for nine flow patterns. The number of runs (second column) listed under the original and transition flow patterns in Table 5 sum to the original number of runs for the basic flow pattern in Table 4 (i.e., the transitional flow patterns in Table 5 are subsets of the basic flow patterns in Table 4). Lastly, the neural network input types of Table 5 are the same as those in Table 4 (i.e., columns 3–10).

Table 5 shows that the lowest success rates occurred using either $\overline{\varepsilon^*}(t)$ or $y_c(t)$ alone as was shown in Table 4. In fact, the success rate using either as a network input was zero for bubbly and bubbly transitional flows. Zero success rates for $\overline{\varepsilon^*}(t)$ and $y_c(t)$ are believed to be due to the challenge of differentiating among the strong similarities between bubbly and bubbly transitional patterns (Figs. 4a, c, 5a, and c). Table 5 shows that the use of $\overline{\varepsilon^*}(t)_{PDF}$, $y_c(t)_{PDF}$, or the group $\langle\overline{\varepsilon^*}(t)\rangle$, $\langle\overline{\varepsilon^*}(t)\rangle_{VAR}$, $\langle\overline{\varepsilon^*}(t)\rangle_{SKEW}$, and $\langle\overline{\varepsilon^*}(t)\rangle_{KURT}$, as input had similar average overall classification success rates (last row) and offered significant improvement in classification success over that of $\overline{\varepsilon^*}(t)$ or $y_c(t)$ for individual flow patterns. This can be attributed to more distinct differences among the PDFs and time averaged statistics for different patterns (PDFs in Figs. 4 and 5 and, for example, the time averaged statistics as represented by the void fraction in Tables 3, 1- $\overline{\varepsilon^*}(t)$. The bottom row of Table 5 shows that the average classification success rate over all flow patterns increases when the time averaged statistics input, $\langle\overline{\varepsilon^*}(t)\rangle$, $\langle\overline{\varepsilon^*}(t)\rangle_{VAR}$, $\langle\overline{\varepsilon^*}(t)\rangle_{SKEW}$, and $\langle\overline{\varepsilon^*}(t)\rangle_{KURT}$, is combined with either of the input values, $\overline{\varepsilon^*}(t)_{PDF}$ or $y_c(t)_{PDF}$. Further, when $\overline{\varepsilon^*}(t)_{PDF}$ and $y_c(t)_{PDF}$ are combined with time average statistics into a single input (column 10), classification success rates greater than 90% were obtained for all patterns. In addition, the average classification success rate over all flow patterns was 98.1%.

The classification success rates for the above nine flow patterns obtained using the combination of time averaged statistics, $\overline{\varepsilon^*}(t)_{PDF}$, and $y_c(t)_{PDF}$ (i.e., column 10) compare well, if not better, than those of past studies involving electrical capacitance measurements (ECT sensors) and horizontal flows. For example, Jeanmeure et al. [23] used an identification tree to classify horizontal flows but only used three patterns. Later, Yan et al. [24] used parameters obtained from steady, two-dimensional numerical simulations of nine flow patterns to train a back-propagation neural network. Their numerical simulations were correlated with experiments involving tomography but did not include the inherent unsteady nature of an actual two-phase flow. In addition, two of their patterns, a tube filled with liquid or empty, were relatively simplistic.

Table 5 lists the classification success rates for the flow patterns but does not specifically characterize the classification errors for the combined input $\langle\overline{\varepsilon^*}(t)\rangle$, $\langle\overline{\varepsilon^*}(t)\rangle_{VAR}$, $\langle\overline{\varepsilon^*}(t)\rangle_{SKEW}$, $\langle\overline{\varepsilon^*}(t)\rangle_{KURT}$, $\overline{\varepsilon^*}(t)_{PDF}$, and $y_c(t)_{PDF}$. An error value within ± 0.5 of zero represents correct identification, otherwise a value outside these bounds is considered to be incorrect. For a total of 546 experiments, a small number (14) were incorrectly classified by one flow pattern and a much smaller number (1) were incorrectly classified by two patterns. More specifically, 99% of the experimental runs were either correctly classified or misclassified by no more than one flow pattern. Tables 4 and 5 together show that the

Table 4
Comparison of Classification Success Rates Using Eight Neural Network Input Vectors for Five Basic Flow Patterns.

Flow Pattern	Number of Runs	$\overline{\varepsilon^*}(t)$	$y_c(t)$	$\overline{\varepsilon^*}(t)_{PDF}$	$y_c(t)_{PDF}$	$\langle\overline{\varepsilon^*}(t)\rangle$ $\langle\overline{\varepsilon^*}(t)\rangle_{VAR}$ $\langle\overline{\varepsilon^*}(t)\rangle_{SKEW}$ $\langle\overline{\varepsilon^*}(t)\rangle_{KURT}$	$\langle\overline{\varepsilon^*}(t)\rangle$ $\langle\overline{\varepsilon^*}(t)\rangle_{VAR}$ $\langle\overline{\varepsilon^*}(t)\rangle_{SKEW}$ $\langle\overline{\varepsilon^*}(t)\rangle_{KURT}$ $\overline{\varepsilon^*}(t)_{PDF}$	$\langle\overline{\varepsilon^*}(t)\rangle$ $\langle\overline{\varepsilon^*}(t)\rangle_{VAR}$ $\langle\overline{\varepsilon^*}(t)\rangle_{SKEW}$ $\langle\overline{\varepsilon^*}(t)\rangle_{KURT}$ $y_c(t)_{PDF}$	$\langle\overline{\varepsilon^*}(t)\rangle$ $\langle\overline{\varepsilon^*}(t)\rangle_{VAR}$ $\langle\overline{\varepsilon^*}(t)\rangle_{SKEW}$ $\langle\overline{\varepsilon^*}(t)\rangle_{KURT}$ $\overline{\varepsilon^*}(t)_{PDF}$ $y_c(t)_{PDF}$
Number of Data in Input Vector for Each Run		250	250	50	50	4	54	54	104
Bubbly	102	100	100	100	100	100	100	100	100
Plug	98	94.9	96.9	100	100	100	100	100	100
Slug	129	86.1	86.1	98.4	99.2	100	99	100	100
St. Wavy	129	94.6	89.1	100	100	99.2	100	100	100
Annular	88	88.6	95.5	97.7	100	98.9	100	100	100
Average Classification Success Rate over All Patterns		92.8%	93.5%	99.2%	99.8%	99.6%	99.8%	100%	100%

Table 5
Comparison of Classification Success Rates Using Eight Neural Network Input Vectors for Nine Flow Patterns.

Flow Pattern	Number of Runs	$\overline{\varepsilon^*}(t)$	$y_c(t)$	$\overline{\varepsilon^*}(t)_{PDF}$	$y_c(t)_{PDF}$	$\langle\overline{\varepsilon^*}(t)\rangle$ $\langle\overline{\varepsilon^*}(t)\rangle_{VAR}$ $\langle\overline{\varepsilon^*}(t)\rangle_{SKEW}$ $\langle\overline{\varepsilon^*}(t)\rangle_{KURT}$	$\langle\overline{\varepsilon^*}(t)\rangle$ $\langle\overline{\varepsilon^*}(t)\rangle_{VAR}$ $\langle\overline{\varepsilon^*}(t)\rangle_{SKEW}$ $\langle\overline{\varepsilon^*}(t)\rangle_{KURT}$ $\overline{\varepsilon^*}(t)_{PDF}$	$\langle\overline{\varepsilon^*}(t)\rangle$ $\langle\overline{\varepsilon^*}(t)\rangle_{VAR}$ $\langle\overline{\varepsilon^*}(t)\rangle_{SKEW}$ $\langle\overline{\varepsilon^*}(t)\rangle_{KURT}$ $y_c(t)_{PDF}$	$\langle\overline{\varepsilon^*}(t)\rangle$ $\langle\overline{\varepsilon^*}(t)\rangle_{VAR}$ $\langle\overline{\varepsilon^*}(t)\rangle_{SKEW}$ $\langle\overline{\varepsilon^*}(t)\rangle_{KURT}$ $\overline{\varepsilon^*}(t)_{PDF}$ $y_c(t)_{PDF}$
Number of Data in Input Vector for Each Run		250	250	50	50	4	54	54	104
Bubbly	52	0	0	94.2	94	94.3	100	98.1	100
Bubbly - T	50	0	0	88	96	76.1	98	96.0	94.0
Plug	58	32.8	31.1	100	97	100	100	98.3	100
Plug - T	40	20.0	22.5	95	98	90.1	100	100	100
Slug	89	29.2	41.6	80	79	94.4	93.3	92.3	96.6
Slug - T	40	17.5	35	65	63	57.5	85	92.5	100
St. Wavy	69	30.4	24.6	52.2	71	81.2	84.1	89.4	97.0
St. Wavy- T	60	13.3	5	67	63	81.7	91.7	90.0	95.0
Annular	88	39.8	28.4	95.5	86	98.9	97.7	98.9	100
Average Classification Success Rate over All Patterns		20.3%	20.9%	81.9%	82.9%	86.0%	94.4%	95.1%	98.1%

In this table, T in the pattern name represents the word "transitional."

input combination of time averaged statistics, $\overline{\varepsilon^*}(t)_{PDF}$, and $y_c(t)_{PDF}$ can be used to reasonably classify flow patterns observed in horizontal flow.

5. Conclusions

This work investigated the use of ECT and neural networks to identify two-phase flow patterns for refrigerant R-134a flowing in a horizontal tube. Laboratory experiments were performed to generate different liquid–vapor flow patterns. High-speed images were recorded for human classification of the flow patterns. The corresponding permittivity data obtained from tomograms was used to train feedforward neural networks to recognize flow patterns. A goal was to classify nine horizontal two-phase flow patterns using neural networks as a predictive tool. Another was to determine which subsets of input data provide high identification success for the flow patterns when analyzed by a neural network. Previous work involving horizontal flows was extended by considering transitional flow patterns associated with four common flow patterns (within a small-diameter tube). A unique feature of the current work is the use of the vertical center of mass coordinate in pattern classification for horizontal flow.

The highest classification success rate occurred with the use of neural network input consisting of $\overline{\varepsilon^*}(t)_{PDF}$, $y_c(t)_{PDF}$, $\langle\overline{\varepsilon^*}(t)\rangle$, $\langle\overline{\varepsilon^*}(t)\rangle_{VAR}$, $\langle\overline{\varepsilon^*}(t)\rangle_{SKEW}$, and $\overline{\varepsilon^*}(t)_{KURT}$. The combination of these data resulted in a 100% success rate for the basic five flow patterns and a high average success rate of 98.1% for nine flow patterns, which include the transitional patterns. In addition, 99% of the experimental runs were either correctly classified or misclassified by only one flow pattern. Based on the success rate of flow pattern identification with relatively small network training and run times, there is potential for the use of ECT combined with neural network analysis to automatically identify two-phase patterns for horizontal flow in thermal process control applications.

References

[1] A.S. Dalkilic, S. Wongwises, Validation of void fraction models and correlations using a flow pattern transition mechanism model in relation to the identification of annular vertical downflow in-tube condensation of R134a, Int. Commun. Heat Mass 37 (2010) 827–834.
[2] H. Caniere, C. T'Joen, A. Willockx, M. De Paepe, Capacitance signal analysis of horizontal two-phase flow in a small tube, Exp. Thermal Fluid Sci. 32 (2008) 892–904.
[3] A. Ghajar, Non-boiling heat transfer in gas–liquid flow in pipes-a tutorial, J. Braz. Soc. Mech. Sci. Eng. 27 (2005) 46–73.
[4] N.P. Ekberg, S.M. Ghiaasiaan, S.I. Abdel-Khalik, M. Yoda, S.M. Jeter, Gas–liquid two-phase flow in narrow horizontal annuli, Nucl. Eng. Des. 192 (1999) 59–80.
[5] W. Qu, S.M. Yoon, I. Mudawar, Two-phase flow and heat transfer in rectangular micro-channels, J. Electron. Packag. 126 (2004) 288–300.
[6] J.M. Quiben, J.R. Thome, Flow pattern based on two-phase frictional pressure drop model for horizontal tubes part II: new phenomenological model, Int. J. Heat Fluid Flow 28 (2007) 1060–1072.
[7] K.A. Triplett, S.M. Ghiaasiaan, S.I. Abdel-Khalik, D.L. Sadowski, Gas–liquid two-phase flow in microchannels part I: two-phase flow patterns, Int. J. Multiphase Flow 25 (1999) 377–394.
[8] W. Warsito, L.S. Fan, Measurement of real-time flow structures in gas–liquid and gas–liquid-solid flow systems using electrical capacitance tomography (ECT), Chem. Eng. Sci. 56 (2001) 6455–6462.
[9] Z. Huang, B. Wang, H. Li, Application of electrical capacitance tomography to the void fraction measurement of two-phase flow, IEEE Trans. Instrum. Meas. 52 (2003) 7–12.
[10] H. Caniere, B. Bauwens, C. T'Joen, M. De Paepe, Mapping of horizontal refrigerant two-phase flow patterns based on clustering of capacitive sensor signals, Int. J. Heat Mass Transf. 53 (2010) 5298–5307.
[11] E. dos Reis, L. Goldstein Jr., Characterization of slug flows in horizontal piping by signal analysis from a capacitive probe, Flow Meas. Instrum. 21 (2010) 347–355.
[12] T. Xie, S.M. Ghiaasiaan, S. Karrila, Artificial neural network approach for flow regime classification in gas–liquid-fiber flows based on frequency domain analysis of pressure signals, Chem. Eng. Sci. 59 (2004) 2241–2251.
[13] E.S. Rosa, R.M. Salgado, T. Ohishi, N. Mastelari, Performance comparison of artificial neural networks and expert systems applied to flow pattern identification in vertical ascendant gas–liquid flows, Int. J. Multiphase Flow 36 (2010) 738–754.
[14] S. Gosh, D.K. Pratihar, B. Maiti, P.K. Das, Identification of flow regimes using conductivity probe signals and neural networks for counter-current gas–liquid two-phase flow, Chem. Eng. Sci. 84 (2012) 417–436.
[15] Y. Mi, M. Ishii, LH. Tsoukalas, Flow regime identification methodology with neural networks and two-phase flow models, Nucl. Eng. Des. 204 (2001) 87–100.
[16] H.L. Hu, J. Dong, J. Zhang, Y.J. Cheng, T.M. Xu, Identification of gas/solid two-phase flow regimes using electrostatic sensors and neural-network techniques, Flow Meas. Instrum. 22 (2011) 482–487.
[17] J.G. Collier, J.R. Thome, Convective Boiling and Condensation, third ed. Oxford University Press, New York, 1994.
[18] Industrial Tomography Systems, Inc., ITS Tomography Toolsuite v7.0 Users Manual, April 2010.

[19] P.J. Kreitzer, M. Hanchak, L. Byrd, Flow Regime Identification of Horizontal two-Phase Refrigerant R-134a Flow Using Neural Networks, Paper IMECE2013-62510, IMECE, San Diego, CA, 2013.
[20] MATLAB r2010a, The MathWorks, Natick, MA, 2010.
[21] J.S. Bendat, A.G. Piersol, Random Data: Analysis and Measurement Procedures, Wiley, New York, 1971.
[22] Wolverine Tube Inc., Engineering Data Book III, 2004 pp. 12–3 to 12–11.

[23] L.F.C. Jeanmeure, T. Dyakowski, W.B.J. Zimmerman, W. Clark, Direct flow-pattern identification using electrical capacitance tomography, Exp. Thermal Fluid Sci. 26 (2002) 763–773.
[24] H. Yan, Y.H. Liu, C.T. Liu, Identification of flow regimes using back-propagation networks trained on simulated data based on a capacitance tomography sensor, Meas. Sci. Technol. 15 (2004) 432–436.